

Probabilistic constrained Bayesian inversion for transpiration cooling

Ella Steins¹  | Tan Bui-Thanh² | Michael Herty³ | Siegfried Müller³ 

¹IRTG Modern Inverse Problems, RWTH Aachen University, Aachen, Germany

²Department of Aerospace Engineering & Engineering Mechanics, The Oden Institute for Computational Engineering & Sciences, Austin, Texas, USA

³Institute for Geometry and Practical Mathematics (IGPM), RWTH Aachen University, Aachen, Germany

Correspondence

Ella Steins, IRTG Modern Inverse Problems, RWTH Aachen University, Schinkelstr. 2, Aachen, Germany.
Email: steins@ices.rwth-aachen.de

Funding information

Deutsche Forschungsgemeinschaft, Grant/Award Numbers: 320021702/GRK2326, 333849990/IRTG-2379, CRC1481, TRR40, HE5386/18-1, HE5386/19-2, HE5386/22-1, HE5386/23-1, 390621612; National Science Foundation, Grant/Award Numbers: NSF-OAC-2212442, NSF-2108320, NSF-1808576, NSF-CAREER-1845799; Department of Energy, Grant/Award Numbers: DE-SC0018147, DE-26083989; 2020 ConTex; 2021 UT-Portugal CoLab

Abstract

To enable safe operations in applications such as rocket combustion chambers, the materials require cooling to avoid material damage. Here, transpiration cooling is a promising cooling technique. Numerous studies investigate possibilities to simulate and evaluate the complex cooling mechanism. One naturally arising question is the amount of coolant required to ensure a safe operation. To study this, we introduce an approach that determines the posterior probability distribution of the Reynolds number using an inverse problem and constraining the maximum temperature of the system under parameter uncertainties. Mathematically, this chance inequality constraint is dealt with by a generalized polynomial chaos expansion of the system. The posterior distribution will be evaluated by different Markov chain Monte Carlo based methods. A novel method for the constrained case is proposed and tested among others on two-dimensional transpiration cooling models.

KEYWORDS

inverse, particle method, porous media, probabilistic methods, transport, uncertainty quantification

1 | INTRODUCTION

In extreme environments such as rocket combustion chambers, transpiration cooling is a promising cooling technique designed to shield the combustion chamber wall from the hot surrounding temperature. A natural arising question for this application is the amount of coolant required to enable a safe operation—here defined as the operation point at which a certain threshold temperature will not be exceeded. For a meaningful risk assessment, we propose to consider parametric uncertainties of the temperature model. At the same time, determining the required amount of coolant is an inverse problem. As the overall research question is therefore an inverse problem subject to probabilistic constraints

This is an open access article under the terms of the Creative Commons Attribution-NonCommercial-NoDerivs License, which permits use and distribution in any medium, provided the original work is properly cited, the use is non-commercial and no modifications or adaptations are made.

© 2022 The Authors. *International Journal for Numerical Methods in Fluids* published by John Wiley & Sons Ltd.

on the maximal temperature, we utilize a combination of generalized polynomial chaos (gPC), a spectral decomposition method, to deal with the probabilistic constraint with an extension of Markov chain Monte Carlo (MCMC) based methods such that the solution of the restricted inverse problem can be sampled.

In the following, we first introduce transpiration cooling (Section 1.1) as well as the used methodologies gPC (Section 1.2) and MCMC (Section 1.3).

1.1 | Transpiration cooling

Efficient cooling concepts are needed in all applications, where materials have to be protected against thermal damage as a result of high thermal loads. Passive cooling for instance uses coating of the material as a heat shield.¹⁻³ We are interested in models for active cooling techniques, like film and transpiration cooling where a coolant is used that transfers heat away from the materials in need of protection. These type of methods generally have a great cooling potential.² Here, transpiration cooling is designed as the injection of a coolant into a hot gas flow through a porous medium. Cooling is achieved by both convection energy within the wall while the coolant passes through the porous medium as well as a coolant film that insulates the wall from the hot gas flow.³

Some applications nowadays considered for transpiration cooling include scramjet combustion chambers,⁴ rocket thrust chambers,⁵ turbine blades,⁶ and others.^{1,7} Even so it has been invented in the 1950s,⁸ due to both advances made in manufacturing and the need for greater cooling efficiency, recently transpiration cooling has come back into the focus of research and has been intensively studied experimentally, analytically and numerically.^{5,9-14}

The porous materials used for transpiration cooling have to meet certain requirements, like high porosity, light-weight, precise geometry, and additionally, for turbine blades,⁶ great material strength. Commonly used types of porous materials are sintered metal or ceramic porous media⁷ and ceramic matrix composites,¹⁵ leaving the pores to be a result of randomness. This in turn leads to negative cooling effects like badly connected pores and demands also suitable simulation techniques to quantify its effect.¹⁶ Additionally, effects of nonuniform permeability have been investigated.¹⁷ Recently, the improved precision of the manufacturing process by additive manufacturing methods has been studied.^{18,19}

For simulation and optimization of transpiration cooling, temperature models^{11,20} and coupled simulations^{5,12} are used. This work originates from the publication by Dahmen et al.⁵ Therein, numerical simulation of transpiration cooling by coupling a porous media flow with a hot gas flow of a rocket combustion chamber is proposed. Numerical experiments in both 2D and 3D are reported. In the following sections, we also focus on the interaction of the coolant with the temperature to allow for the treatment of, for example, temperature constraints. Alternative detailed injection models are based on turbulence modeling, heuristic considerations, and direct numerical simulations.^{14,21-23}

1.2 | Generalized polynomial chaos

We propose to consider a model with uncertain parameters to acknowledge for the uncertainties present in the production of the porous material and the simulation of the flow as well as the so far missing detailed physical model for the interaction of flow and porous media and the presence of inequality requirements for the temperature. Which parameters should be considered uncertain depends on two aspects, namely, model knowledge and sensitivity. Model knowledge here refers to the practitioners knowledge of uncertainties of the process, for example, the manufacturing process of the porous material that results in an uncertain porosity. The importance of a sensitivity analysis of the relevant output, here the temperature, with respect to potential uncertain parameters is discussed in Reference 24. The idea is to consider only those uncertain parameters that critically influence the output.

We shortly introduce the key idea of gPC here without going into too much detail. A more formal notation is given in Section 2 for the used transpiration cooling model.

Assuming that the output has a finite variance, gPC expands the stochastic variable output y with respect to orthogonal basis polynomials Φ such that

$$y(\xi) = \sum_{i=0}^{\infty} \hat{y}_i \cdot \Phi_i(\xi), \quad (1)$$

where \hat{y}_i are deterministic coefficients.

The idea was first presented by Wiener²⁵ where Φ_i are Hermite polynomials. Cameron and Martin²⁶ proved that the series expansion is convergent for every process with finite second statistical moments where $\|\sum_{i=0}^P \hat{y}_i \cdot \Phi_i(\xi) - y\|_{L^2} \rightarrow 0$ for $P \rightarrow \infty$.

The original work by Ghanem and Spanos²⁷ considers stochastic finite element systems by using the Karhunen–Loève expansion. Ghanem extended this idea to model stochastic finite element systems for probabilistic transport in porous media with Gaussian parametric uncertainties ξ .²⁸ Xiu and Karniadakis²⁹ later extended the polynomial chaos expansion to various input probability distributions, where they summarize the choice of the basis polynomials as in Table 1.

In order to compute the deterministic coefficients \hat{y} of the gPC expansion in Equation (1), either intrusive^{30,31} or non-intrusive methods^{32,33} are available. Intrusive methods insert (1) into the model equations while nonintrusive methods are based on a set of evaluations of the deterministic model $\{y(\xi^0), y(\xi^1), \dots, y(\xi^N)\}$.³⁴ We describe the chosen coefficient estimation method for transpiration cooling after introducing the model in Section 2.

Furthermore, in practice the series expansion is truncated after a finite number of terms. Choosing the truncation order necessary for a set accuracy is a model-specific process. The well-known leave-one-out cross validation (LOOCV) method is suggested in Reference 35 to test the performance of the gPC expansion. This procedure is especially useful when using a regression method to estimate the coefficients as then the training and test sets for the LOOCV method are readily available.

1.3 | Markov chain Monte Carlo

As the evaluation of the temperature constraint in transpiration cooling requires the full probability distribution of the temperature, we propose here a gPC expansion. At the same time, optimizing the cooling effect by choosing a suitable Reynolds number while using the pressure as a simulation output, is formulated as an inverse problem.

Inverse problems can be addressed using either a deterministic or statistical approach. In this article, we choose the latter using the Bayesian inversion framework which treats the unknown solution as a random variable whose posterior probability distribution is provided by Bayes' theorem.³⁶ However, exploring the posterior can be challenging especially for high-dimensional inputs and non-Gaussian posteriors. Sampling strategies such as MCMC,³⁷ though computationally expensive, can be used to generate samples from the target posterior. Alternatively, sequential Monte Carlo (SMC) can be used which moves a set of samples (called particles) until the set's histogram represents the desired output distribution.³⁸ Due to the complication arising from the probabilistic constraint that renders other methods infeasible or difficult, we adopt an MCMC approach.

MCMC methods consist in general of two steps. First, candidate points are suggested based on a proposal distribution. In a second step, the candidate points are then either accepted or rejected with a probability given by the acceptance ratio. In case of rejection the current sample is added to the Markov chain again whereas the Markov chain moves to the candidate point for acceptance case. This two-step procedure is repeated, until enough samples are collected such that the Markov chain converges to the desired distribution.

The choice of the proposal distribution sets MCMC methods apart. The Metropolis–Hastings algorithm (MHA), for example, in Reference 39, uses a random walk centered on the current sample. In order to more effectively move along the shape of the target measure, the Hamiltonian Monte Carlo (HMC)⁴⁰ proposes the next candidate point based on the gradient of the target distribution. This idea is also exploited in the Stein variational gradient descent (SVGD) algorithm⁴¹ where a set of particles is moved based on the gradient information.

TABLE 1 Correspondence of polynomial basis to input distribution²⁹

	Distribution of random variables ξ	Wiener–Aksey chaos $\{\Phi(\xi)\}$	Support of ξ
Continuous	Gaussian	Hermite	$(-\infty, \infty)$
	Gamma	Laguerre	$[0, \infty)$
	Beta	Jacobi	$[a, b]$
	Uniform	Legendre	$[a, b]$

Furthermore, for computing the acceptance ratio, the posterior at both the current sample and the proposed candidate is evaluated. One option is to choose the acceptance ratio such that the detailed balance equation is fulfilled. This guarantees that the sampled distribution is the stationary distribution which in turn is the target distribution in the limit.

In general, the convergence rate depends on the choice of tuning parameters, for example, the variance of the random walk or the step width for gradient-based methods. The interested reader is referred to, for example, Reference 36 where a set of methods are described.

Bayesian inverse problem is a wide research field, and we here only review literature on the constrained case. Wu et al.⁴² extend Bayesian inversion by incorporating an additional likelihood to the Bayesian inversion based on fitness of the solution to the constraint.

Another approach is presented in the context of Bayesian optimization in the machine learning community. Here, in order to globally optimize black-box derivative-free methods, a statistical Gaussian surrogate for the objective function is built upon Gaussian process regression.⁴³ An acquisition function is derived from the surrogate and extended to the constrained optimization problems in References 44 and 45.

We extend three aforementioned mentioned methods—MHA, HMC, and SVGD—to the constrained case in Section 3.1.1 and comment on the hyperparameter tuning as well as analyze their convergence in Section 4.4.

The rest of this article is structured as follows: In Section 2, the two models for transpiration cooling are presented and the extension to the stochastic system is given. Section 3 then introduces the solution method, a novel constrained random walk MCMC method, and two alternative solution methods for comparison. Following this, the numerical results are discussed in Section 4.

2 | MODELING TRANSPIRATION COOLING AT AN INTERFACE

Notation. In the following sections, all random variables (RV) \mathbf{X} are given in bold type and realizations are X . We assume each RV \mathbf{X} has a probability density denoted by $\Pi(\mathbf{X})$. Data are denoted by the suffix ^{data}.

The dimensionless *forward problem* consists of two coupled ordinary differential equations (ODEs), one for the fluid temperature $T_f = T_f(x; \mathbf{Re})$, one for the solid temperature $T_s(x; \mathbf{Re})$ of a spatially 1D strip porous media of normalized length $x \in [0, 1]$. Here, \mathbf{Re} is the uncertain Reynolds number.* The third ODE describes the evolution of the density ρ_f of the coolant, where $\rho_f'(x; \mathbf{Re}) = \frac{d\rho_f(x; \mathbf{Re})}{dx}$. The velocity of the coolant is denoted by $v(x)$, $x \in [0, 1]$.

$$T_s'(x; \mathbf{Re}) = \frac{\kappa_f}{(1 - \phi) \cdot \kappa_s} \mathbf{Re} \cdot Pr_f \cdot (T_f(x; \mathbf{Re}) - T_{\text{HG}}) + \frac{q}{(1 - \phi) \cdot \kappa_s}, \quad (2a)$$

$$T_f'(x; \mathbf{Re}) = \frac{Nu_{v,f}}{Pr_f \cdot \mathbf{Re}} \cdot (T_s(x; \mathbf{Re}) - T_f(x; \mathbf{Re})), \quad (2b)$$

$$\rho_f'(x; \mathbf{Re}) = N(x; \mathbf{Re}) \cdot \rho_f(x; \mathbf{Re}) \quad (2c)$$

with

$$N(x; \mathbf{Re}) = \frac{\frac{Nu_{v,f}}{\mathbf{Re} \cdot Pr_f} \rho_f^2(x; \mathbf{Re}) (T_s(x; \mathbf{Re}) - T_f(x; \mathbf{Re})) + \left(\frac{L^2}{\mathbf{Re} \kappa_D} + \frac{L}{\kappa_F} \right)}{\phi^{-2} - \rho_f^2(x; \mathbf{Re}) T_f(x; \mathbf{Re})},$$

$$v(x; \mathbf{Re}) = \frac{1}{\rho_f(x; \mathbf{Re})}. \quad (2d)$$

The pressure at the interface is denoted by p and

$$\mathbf{p} := p_f(x = 1; \mathbf{Re}) = T_f(x = 1; \mathbf{Re}) \cdot \rho_f(x = 1; \mathbf{Re}) \quad (2e)$$

and the initial conditions are given by

$$T_f(0; \mathbf{Re}) = T_c, \quad T_s(0; \mathbf{Re}) = T_b, \quad \rho_f(0; \mathbf{Re}) = \frac{P_R}{T_c}. \quad (2f)$$

Details on the 1D model can be found in References 46 and 47. For this system (2a)–(2f), the other model parameters are given in Table A1 in the Appendix.

The *deterministic forward problem* is summarized as

$$\mathbf{p} := F(\mathbf{Re}), \quad (3)$$

where the pressure $\mathbf{p} := p_f(x = 1; Re)$ in (2e) is observable at the position $x = 1$. Observations of the pressure are denoted by p^{data} and are drawn from a numerical integration of Equations (2a)–(2f) of the coolant through a porous material with superposed white noise. The physical relations are described by the operator F which is comprised of a differential-algebraic system of equations.

We will first consider the spatially homogeneous situation, where we refer to (2a)–(2f) as *model 1*. The constraint $T_f(x = 1; Re) \leq T_{\max}$ will then be imposed on the temperature T_f .

In a second step, we extend the problem to the nonhomogeneous case, here referred to as *model 2*. We consider a porous media with elongation $z \in (d_1, d_2)$ divided in two sections, where each section consists of finitely many vertical 1D pores as indicated in Figure 1. Each vertical strip is parameterized by $x \in (0, 1)$. Both sections have their own deterministic porosity ϕ_j , $j = 1, 2$; but the *same* uncertain Reynolds number \mathbf{Re} . This geometry is common, see Reference 48. At the boundary of the porous media we assume solid material with a possibly high initial temperature $T_0 > T_{\max}$. We are interested in the evolution of the temperature $T_h(z, t)$ at the interface of the porous material with the surrounding conditions over time t . In our model, this temperature is obtained from the porous media equations at $x = 1$.

The temperatures $T_h(z_i, t = 0) = T_f^i(x = 1; \mathbf{Re})$ at different locations $z_i \in (0, 1)$, $i = 1, \dots, N$, are then given by *model 1* (2a)–(2f) with porosity ϕ_i . Here, we denote by $T_f^i(x = 1; \mathbf{Re})$ the solution to (2a)–(2f) for fixed porosity ϕ_j . Across the interface z the evolution of the temperature is assumed to be given by the linear heat diffusion equation with known deterministic diffusion coefficient $\lambda > 0$:

$$0 = \frac{\partial T_h(z, t)}{\partial t} - \lambda \frac{\partial^2 T_h(z, t)}{\partial z^2}, \quad z \in [0, 1], \quad t \geq 0. \quad (4a)$$

The initial condition is given by the temperature obtained by the 1D strip, see (4b), where we assume the porous media pores are of size Δz :

$$T_h(z, t = 0) = \begin{cases} \sum_{i=d_1}^{d_2} \chi_{[z_i - \Delta z, z_i + \Delta z]}(z) T_f^i(x = 1; \mathbf{Re}) & z \in (d_1, d_2) \subset [0, 1], \\ T_0 & \text{otherwise} \end{cases} \quad (4b)$$

and Neumann boundary conditions at $z = 0$ and $z = 1$, respectively.

The constraint will be imposed at a fixed terminal time $t = t_c$ and hence reads

$$T_h(z, t = t_c) \leq T_{\max} \quad \forall z \in [0, 1]. \quad (5)$$

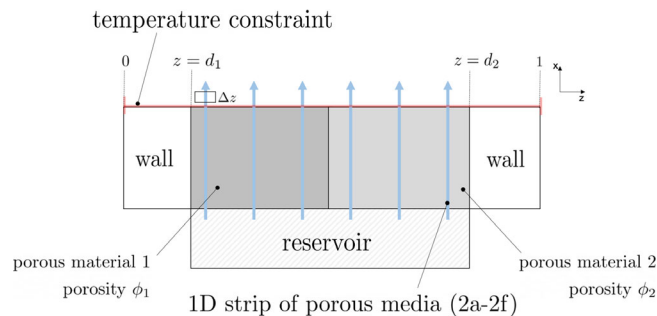


FIGURE 1 The setup of *model 2* and *model 3*. Two porous materials with different porosities are considered, and sixty 1D strip simulations are performed to derive the spatially dependent temperature at the interface. Across z , the evolution of the temperature is assumed to be given by the heat equation. The temperature constraint is imposed over the whole length of z at some time $t = t_c > t_0$. [Colour figure can be viewed at wileyonlinelibrary.com]

Incorporating model uncertainties into the design is crucial for substantively design and risk assessment. The porosity ϕ , respectively, is a result of a manufacturing process where the porous material breaks at random spots.¹⁹ The heat flux \mathbf{q} is random itself as a product of the randomness of the porous material. A sensitivity analysis of the model showed the highest sensitivity of the temperature toward uncertainties in $(\mathbf{Re}, \phi, \mathbf{q})$. For the one-dimensional model, the heat flux \mathbf{q} and the porosity ϕ will be treated as parametric uncertainties. For *model 2*, we can account for a spatial uncertainty by modeling two sections with separate deterministic porosities but the same uncertain heat flux \mathbf{q} . Lastly, *model 3* additionally incorporates spatially uncertain heat flux with RVs $\mathbf{q}_1, \dots, \mathbf{q}_N$.

Even so the following discussion is not limited to this case, we assume normally distributed uncertainties, with $\mathbf{q} \sim \mathcal{N}(q_0, \sigma_q^2)$ and $\phi \sim \mathcal{N}(\phi_0, \sigma_\phi^2)$.

As the parametric uncertainties of the heat flux and the porosity enter the temperature, T_f and T_h also become RVs, that is, $T_f = T_f(x, \mathbf{q}, \phi; \mathbf{Re})$. To formalize, we assume that (\mathbf{q}, ϕ) is a RV defined on a probability space $(\Omega, P(\Omega); \mathbb{P})$ mapping to \mathbb{R}^2 .

For each fixed $(x, Re) \in (0, 1) \times \mathbb{R}^+$ we additionally assume that $T_f(x, \cdot, \cdot; Re) \in L^2(\Omega; \mathbb{R})$. We apply a gPC expansion to the system of ODEs governing the temperature evolution in the porous media. Denote by $\mu_1(q)dq$ and $\mu_2(\phi)d\phi$ the probability measures of the independent RVs \mathbf{q} and ϕ , respectively. Then, we define for $d\nu(q, \phi) = \mu(q)\mu_2(\phi)dqd\phi$ and $y_i \in L^2_\nu(\Omega; \mathbb{R})$ the inner product

$$\langle y_1, y_2 \rangle = \int_{-\infty}^{+\infty} \int_{-\infty}^{+\infty} y_1(\tilde{q}, \tilde{\phi}) \cdot y_2(\tilde{q}, \tilde{\phi}) d\nu(\tilde{q}, \tilde{\phi}). \quad (6)$$

Then, for any $y \in L^2_\nu(\Omega; \mathbb{R})$ we have $\|\sum_{k=0}^K \bar{y}_k \cdot \tilde{\Phi}_k(q, \phi) - y\|_{L^2_\nu} \rightarrow 0, K \rightarrow \infty$, where \bar{y}_k is the Galerkin projection onto the space spanned by the polynomials $\tilde{\Phi}_0, \dots, \tilde{\Phi}_N$. The previous expansion is the gPC expansion and we apply it to $T_f(x, \mathbf{q}, \phi; Re)$. Since (\mathbf{q}, ϕ) are independent RV we have after possible normalization that $\tilde{\Phi}_k(q, \phi) = \Phi_k(q)\Phi_k(\phi)$.

The coefficients \hat{T}_{ij} are determined by solving

$$\frac{d}{dx} \hat{T}_{ij}^f = \frac{1}{\langle \Phi_i^2, \Phi_j^2 \rangle} \int_{-\infty}^{\infty} \int_{-\infty}^{\infty} \frac{Nu}{RePr} (T_s^K - T_f^K) d\phi dq, \quad (7a)$$

$$\frac{d}{dx} \hat{T}_{ij}^s = \frac{1}{\langle \Phi_i^2, \Phi_j^2 \rangle} \int_{-\infty}^{\infty} \int_{-\infty}^{\infty} \frac{\kappa_f}{(1-\phi)\kappa_s} RePr (T_f^K - T_{HG}) + \frac{q}{1-\phi} \kappa_s d\phi dq, \quad (7b)$$

where $T_s^K = \sum_{i,j=0}^K \hat{T}_{ij}^s(x; Re)\Phi_i(q)\Phi_j(\phi)$, $T_f^K = \sum_{i,j=0}^K \hat{T}_{ij}^f(x; Re)\Phi_i(q)\Phi_j(\phi)$,

$$\hat{T}_{ij}^0 = \begin{cases} T_c, & i=j=1 \\ 0, & \text{otherwise} \end{cases} \quad \text{and similarly} \quad \hat{T}_{ij}^s = \begin{cases} T_b, & i=j=1 \\ 0, & \text{otherwise.} \end{cases}$$

Numerically, an explicit Euler scheme is used in Section 4 as well as stochastic collocation to approximate the integrals. The gPC expansion of the temperature $T_h(z, t)$ can be obtained using also a gPC expansion of Equation (4a).

3 | SOLUTION METHOD

In this section, the framework of probabilistic constrained Bayesian inversion is introduced. A solution method based on a combination of gPC and constrained MCMC is proposed. The method is explained in the general setting for notational brevity and clarity. In Section 4, it will be applied to the transpiration cooling problem.

In the following section the finite dimensional optimization parameter is $\theta \in \mathbb{R}^{N_\theta}$. Let $(\Omega, F(\Omega), \mathbb{P})$ be a probability space and $\bar{\xi} : \Omega \rightarrow \mathbb{R}^d$ a RV with Lebesgue probability density Π . For a deterministic function $\bar{f} : \mathbb{R}^d \rightarrow \mathbb{R}^{N_f}$ we have in case of random input $\bar{f}(\bar{\xi}(\omega))$ for $\omega \in \Omega$. A change of variables $\bar{\xi}(\omega) \rightarrow \xi$ gives the considered representation $\bar{f}(\xi) : \mathbb{R}^d \rightarrow \mathbb{R}^{N_f}$.

3.1 | Problem formulation

In the considered case we denote by $f_1 : \mathbb{R}^{N_\theta} \times \mathbb{R}^d \rightarrow \mathbb{R}$ a forward model depending on an optimization parameter θ as well as the RV $\xi = \bar{\xi} \in \mathbb{R}$. Similarly, we assume that $f_2 : \mathbb{R}^{N_\theta} \times \mathbb{R}^d \rightarrow \mathbb{R}$ models possible point wise inequalities.

As in a Bayesian framework, we assume given prior information as probability density of the parameter $\Pi_{\text{prior}}(\theta)$. Let f_1 be observable with RV $\mathbf{f}_1^{\text{data}} = f_1(\xi^*, \theta^*) + \boldsymbol{\eta}$ with variance σ_l^2 , where $\boldsymbol{\eta}$ is white noise, $\theta^* \in \mathbb{R}^{N_\theta}$ is an unknown parameter, and $\xi^* \in \mathbb{R}^d$ an unknown realization. We comment on the data generation for the numerical examples in Section 3.1.1.

As in, for example, Reference 42, the likelihood function $\Pi_l : \mathbb{R}^{N_f} \rightarrow \mathbb{R}$ is defined by

$$\Pi_l(\mathbf{f}_1^{\text{data}} | \theta) := \frac{1}{\sqrt{2\pi\sigma_l}} \cdot e^{-\frac{1}{2\sigma_l^2} \sum_{i=1}^{N_f} (f_{1,i}^{\text{data}} - f_1(\mathbb{E}_\xi, \theta))^2}. \quad (8)$$

Here, $f_{1,i}^{\text{data}}$ are N realizations of RV $\mathbf{f}_1^{\text{data}}$. The model output f_1 is computed with respect to the expectation $\mathbb{E}_\xi = \int \xi \Pi_\xi(\xi) d\xi$, as for the Bayesian Inversion only the parameter θ is optimized. The optimization of this parameter has the goal of finding realizations which will be used in the operation of the cooling mechanism. For example, the mass flow of the coolant can be adjusted. Since an optimality for a single parameter is not desired from an application point of view, we are interested in the optimal probability distribution $\Pi(\theta)$ of this parameter θ . The associated RV is θ .

In contrast to that we have parametric uncertainties, labeled ξ . The porosity, for example, is a RV as the manufacturing process is inherently uncertain and thus not controllable.

These parametric uncertainties come into play as for some fixed threshold β the risk that $f_2(\xi; \theta) \leq \beta$ is not satisfied in face of the parametric uncertainties ξ for the optimized realization θ should be lower than α .

Thus, the goal is to determine the constrained posterior $\Pi_{\text{post}}^c(\theta)$ such that the probability $\mathbb{P}_\xi(f_2(\xi; \theta) \leq \beta) \geq \alpha$ a.s. w.r.t. θ . Here, α is our risk. We propose now to obtain such a (posterior) distribution $\Pi_{\text{post}}^c(\theta)$ by restricting the admissible set for $\theta \in \mathbb{R}^{N_\theta}$ such that the constraint is fulfilled: Define

$$S := \{ \theta \in \mathbb{R}^{N_\theta} : \mathbb{P}_\xi(f_2(\xi; \theta) \leq \beta) \geq \alpha \} \quad (9)$$

as the subset for which the constraint is fulfilled. Then, the constrained posterior can be expressed as

$$\Pi_{\text{post}}^c(\theta) = c \cdot \mathcal{X}_S(\theta) \cdot \Pi_{\text{prior}}(\theta) \cdot \Pi_l(\mathbf{f}_1^{\text{data}} | \theta), \quad (10)$$

where \mathcal{X}_S is the characteristic function on the set S and c is a normalization constant.

Numerically, the problem (10) requires an efficient description of the set S of the constraints. We propose using a gPC expansion of $f_2 = \sum_{i=0}^{\infty} \hat{f}_{2,i} \Phi_i(\xi)$ in ξ . This leads for any fixed realization $\theta \in \mathbb{R}^{N_\theta}$ to

$$\mathbb{P}_\xi(f_2(\xi; \theta) \leq \beta) = \int_{\mathbb{R}^d} \left\{ \begin{array}{ll} 1 & \text{if } \sum_{i=0}^{\infty} \hat{f}_{2,i}(\theta) \Phi_i(\xi) \leq \beta \\ 0 & \text{otherwise} \end{array} \right\} \Pi(\xi) d\xi. \quad (11)$$

Hence, the set S is given by $S = \{ \theta \in \mathbb{R}^{N_\theta} : \int_{\mathbb{R}^d} \{ \} \Pi(\xi) d\xi \geq \alpha \}$.

Remark 1. In a Bayesian setting, an expansion of f_2 in (ξ, θ) would return a global cheap-to-evaluate meta model. However, this is not accurate as only prior knowledge of the optimization parameter is known⁴⁹ and thus no true input probability distribution needed for propagating the uncertainties is available. Therefore, here the gPC expansion still depends on realizations θ which comes at a larger computational cost but higher accuracy.

3.1.1 | Data generation

We here generate the data for the observable pressure as $\mathbf{f}_1^{\text{data}} = f_1(\xi^*, \theta^*) + \boldsymbol{\eta}$, where the realizations ξ^* are drawn from the given input noise Π_ξ and $\boldsymbol{\eta}$ is the measurement noise.

The realization θ^* is sampled from the prior distribution Π_{prior} . Note that choosing a meaningful prior is an active research question in itself. Gaussian priors are probably the most commonly used class of prior distributions.³⁹ In the first numerical example we consider a Gaussian prior. Here, the variance of the prior is chosen to be quite high, reducing the influence of the prior. To test different prior assumptions, the prior is chosen to be uniformly distributed in the second and third numerical examples.

If experimental data is available, the noise η can be set to match the measurement error which is usually known. Here, it is chosen to be a lower percentile (1%–2%) of the absolute output f_1 (the pressure at the interface).

3.1.2 | Constrained random walk MCMC

The MHA³⁹ is a MCMC method characterized by using a random walk as a proposal distribution. Here, it is modified to incorporate the constraint by further using an indicator function to compute the ratio, following the approach described above from Gardner and Gelbert.^{44,45} The pseudo-code is given in Algorithm 1 as an extension to the unconstrained algorithm presented in Reference 39, and labeled constrained Random Walk (cRW) MCMC.

Algorithm 1. Constrained random walk (cRW) Markov chain Monte Carlo

Given: σ and initial value θ_0

for $i = 0, \dots, N - 1$ **do**

Draw candidate $\theta^* | \theta_i$, where $\theta^* \sim \mathcal{N}(\theta_i, \sigma^2)$

$$\chi(\theta^*) = \begin{cases} 1 & \text{if } P_{\xi}(f_2^{gPC}(\xi; \theta^*) \leq \beta) \geq \alpha \\ 0 & \text{otherwise} \end{cases}$$

$$\alpha_1 = \chi_S(\theta^*) \cdot \min \left(1, \frac{\Pi_l(\theta^*) \cdot \Pi_{\text{prior}}(\theta^*)}{\Pi_l(\theta_i) \cdot \Pi_{\text{prior}}(\theta_i)} \right)$$

end for

if $\alpha_1 = 1$: **then**

Accept candidate and set $\theta_{i+1} = \theta^*$

else

Accept candidate and set $\theta_{i+1} = \theta^*$ with probability α_1 , else reject and set $\theta_{i+1} = \theta_i$

end if

In order to describe the method it is sufficient to state the transition kernel $K : \mathbb{R}^{N_\theta} \rightarrow \mathbb{R}^{\geq 0}$:

$$K(\theta, \theta^*) = \alpha(\theta, \theta^*), \quad \alpha(\theta, \theta^*) = \min \left\{ 1, \frac{\Pi_{\text{prior}}(\theta^*) \cdot \Pi_l(\theta^*)}{\Pi_{\text{prior}}(\theta) \cdot \Pi_l(\theta)} \cdot \chi_S(\theta^*) \right\}, \quad (12)$$

where θ is a current sample and θ^* is a candidate point proposed by the random walk. The indicator function χ_S and S are defined by Equation (9).

Theorem 1. *The cRW transition kernel K (12) satisfies the detailed balance condition with target measure $\Pi_{\text{post}}^c(\theta)$ (10) given a feasible initial sample θ .*

Proof. The detailed balance equation reads as

$$\Pi_{\text{prior}}(\theta^*) \cdot \Pi_l(f_1^{\text{data}} | \theta^*) \cdot K(\theta^*, \theta) = \Pi_{\text{prior}}(\theta) \cdot \Pi_l(f_1^{\text{data}} | \theta) \cdot K(\theta, \theta^*). \quad (13)$$

For any two samples, where $\chi(\theta^*) = \chi(\theta)$ the above statement is true. In case of $\chi(\theta^*) = \chi(\theta) = 1$, (13) simplifies to the standard detailed balance equation for random walk. If the indicator function for both samples is zero, so is the probability of either sampling one of them zero.

In case $\chi(\theta^*) = 0$ and $\chi(\theta) = 1$, the suggested point is not within the feasible region of the *constrained* posterior Π_{post}^c , and will thus not be sampled. The rejection will lead to a repetition of the current sample θ . ■

3.1.3 | Alternative solution methods for numerical comparisons

Alternative Monte Carlo based sampling methods use the gradient information of the posterior to propose new candidate points with the goal to achieve higher acceptance rates. We consider two different gradient descent algorithms, the HMC⁴⁰ and, as an interacting particle system, the SVGD introduced by Liu and Wang.⁴¹

In this work, in order to treat the constrained posterior, we propose to introduce a penalty term. The gradient of the log-posterior is therefore supplemented by a modification $\nabla\mathcal{H}$, such that the gradient is given by

$$\nabla\mathcal{G}(\theta) = \nabla \log(\Pi_{\text{prior}}(\theta) \cdot \Pi_l(\theta)) + \nabla\mathcal{H}(\theta), \quad (14a)$$

with

$$\nabla\mathcal{H}(\theta) = \begin{cases} \delta, & \text{if } \theta \notin \mathcal{S}, \\ 0, & \text{otherwise,} \end{cases} \quad (14b)$$

where δ is a hyperparameter used to avoid sampling in the unfeasible area. The pseudo-codes for the extended methods are given in Algorithms 2 and 3 as extensions of the unconstrained algorithms presented in References 40 and 41. They are labeled constrained Hamiltonian Monte Carlo (cHMC) and constrained Stein variational gradient descent (cSVGd), respectively.

It should be noted the detailed balance equation is not fulfilled for the cHMC algorithm due to the modification.

Algorithm 2. Constrained Hamiltonian Monte Carlo (cHMC)

Given: \mathcal{G} , Π_{prior} , Π_l , L , s , M and initial value θ_0

for $i = 0, \dots, N - 1$ **do**

Draw $\tilde{m} \sim \mathcal{N}(0, M)$ and $L_1 \sim \mathcal{U}(1, L)$

Let $\theta_0 = \theta_i$ and $\tilde{m}_0 = \tilde{m} + \frac{s}{2} \nabla\mathcal{G}(\theta)|_{\theta_0}$

for $j = 1, \dots, L_1$ **do**

Leapfrog-Integration

$\theta_j = \theta_{j-1} + s \cdot M^{-1} \cdot \tilde{m}_j$

$\tilde{m}_j = \tilde{m}_{j-1} + s \cdot \nabla\mathcal{G}(\theta)|_{\theta_j}$

end for

$\theta^* = \theta_{L_1}$

$\tilde{m}^* = \tilde{m}_{L_1-1} - \frac{s}{2} \nabla\mathcal{G}(\theta)|_{\theta^*}$

compute acceptance ratio:

$\alpha_1 = \min \left(1, \exp \left[\log(\Pi_{\text{prior}}(\theta^*) \cdot \Pi_l(\theta^*)) - \frac{1}{2} M^{-1} (\tilde{m}^*)^2 - \log(\Pi_{\text{prior}}(\theta) \cdot \Pi_l(\theta)) + \frac{1}{2} M^{-1} (\tilde{m})^2 \right] \right)$

if $\alpha_1 = 1$ **then**

Accept candidate and set $\theta_{i+1} = \theta^*$

else

Set $\theta_{i+1} = \theta^*$ with probability α_1 , else reject and set $\theta_{i+1} = \theta_i$.

end if

end for

Algorithm 3. Constrained Stein variational gradient descent (cSVGd)

Given: \mathcal{L} , a RBF kernel k , initial step size s_1 , and a set of initial particles $\{\theta_i^0\}_{i=1}^{N_1}$

for $l = 0, \dots, N_2 - 1$ **do**

$\theta_i^{l+1} = \theta_i^l + s_l \left(\frac{1}{n} \sum_{j=1}^n \left[k(\theta_j^l, \theta) \nabla_{\theta_j^l} \mathcal{L}(\theta_j^l) + \nabla_{\theta_j^l} k(\theta_j^l, \theta) \right] \right)$

end for

4 | COMPUTATIONAL RESULTS

4.1 | Space-homogeneous transpiration cooling

For model 1, flow through the porous medium is simulated. Two stochastic input parameters are considered, which are both assumed to be normally distributed with $\phi \sim \mathcal{N}(\phi_0, \sigma_\phi^2)$ and $q \sim \mathcal{N}(q_0, \sigma_q^2)$. The prior of the Reynolds number is assumed to be a Gaussian prior with $\mathcal{N}(\mu_p, \sigma_p^2)$. While the pressure is observable, the temperature is constrained.

For the cHMC and cSVGD, the use of the log-posterior avoids overflow and underflow in the computation of the ratio for the acceptance rate.⁵⁰ Furthermore, the particles are following a smoothed gradient. For this model, the gradient can be derived analytically and is given by

$$\begin{aligned} & \nabla_{Re} \log \left(\Pi_{\text{prior}}(Re) \frac{1}{N} \prod_{i=0}^N \Pi_l(p_i(\phi_0)|Re) \right) \\ &= -\frac{(Re - \mu)}{\sigma_p^2} + (\nabla_{Re} p(Re)) \frac{1}{N \sigma_l^2} \sum_{i=0}^N (p_i^{\text{data}} - p(Re)), \end{aligned} \quad (15)$$

where $(\nabla_{Re} p(Re))$ is evaluated using first-order finite differences. As the derivation with respect to a single input, the Reynolds number, is considered, two evaluations of the ODE are needed for finite differences. Therefore, using an adjoint gradient would not be more efficient to use.

Figure 2 shows the sampled constrained posterior probability distribution using cRW, cHMC, and cSVGD. The results reproduce the true posterior. It can be seen that for lower Reynolds numbers the temperature constraint is not fulfilled as not enough coolant is injected to decrease the temperature at the interface with the desired probability of 95%.

While the cRW is using a hard constraint formulation to sample the constrained posterior, the cSVGD and cMHA violate the constraint requirement based on the choice of the penalization parameter δ . Therefore, if a weak penalization is chosen in (14b), not all samples might be within the feasible region. On the other hand, the modification alters the shape of the posterior and if δ is chosen to be very large, it will affect the sampling at the edge of the feasible region. The nonfeasible samples may be removed by checking the constraint in a post-processing step, however this new distribution does not resemble the Markov chain.

The temperature is increasing as the mass flow of the coolant and thus the Reynolds number increases. Therefore, Figure 2 shows that in this scenario, the chance constraint is concomitantly a box constraint. In such a case, a projected gradient method can be used instead of the modification. This circumvents the downsides of the modification as described above, where the shape of the posterior is altered, and samples without the feasible region might be removed in a post-processing step. However, in the general case given in (10), the secondary condition does not necessarily resemble a box constraint and the use of a projected gradient method might not be possible.

The projected gradient method has been combined with the SVGD for demonstration purposes. In case where $S = \{\theta \geq \theta_{\text{crit}}\}$, we can reformulate (10) as

$$\Pi_{\text{prior}}(\theta) \cdot \Pi_l(f_1^{\text{data}}|\theta) \text{ s.t. } \theta \geq \theta_{\text{crit}}. \quad (16)$$

For every particle $\{\theta_k^j\}_{k=1}^m$ in the j th generation of the algorithm with a set of m particles, the known SVGD proposal step is performed. The gradient of the unconstrained posterior at θ_k^j is then projected back onto the feasible region by a projection step

$$d_k^j = \Pr(\theta_k^j + \nabla_{\theta} \log \Pi_{\text{prior}}(\theta_k^j) \cdot \Pi_l(\theta_k^j)) - \theta_k^j. \quad (17)$$

Finally, the particles are then updated by $\theta_k^{j+1} = \theta_k^j + s^j \cdot d_k^j$, where s is the current SVGD step size.

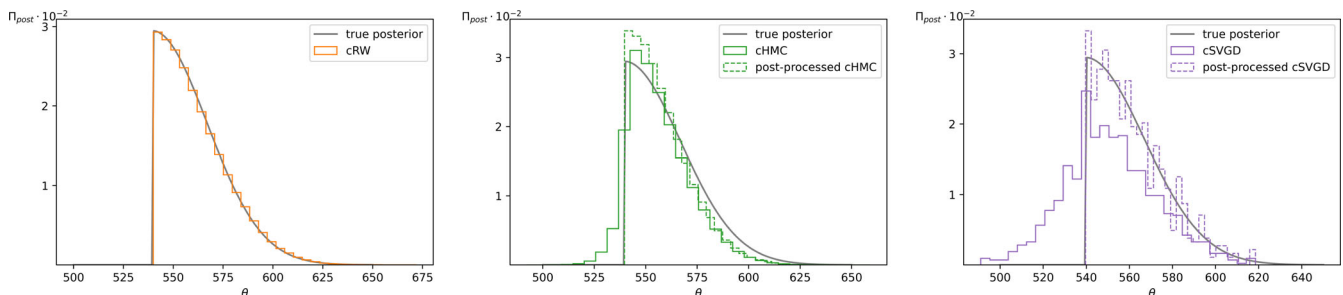


FIGURE 2 Histograms model 1: The results of the cRW, the cHMC, and the cSVGD can be seen from left to right. Additionally to the Markov chain, post-processed versions are shown for the cHMC and cSVGD. Here, unfeasible samples have been removed from the corresponding Markov chains. For comparison, the true posterior (gray line) is plotted as well. It can be seen that for a Reynolds number less than 540, the temperature constraint is not fulfilled. The set S is $\{\theta \geq 540\}$. [Colour figure can be viewed at wileyonlinelibrary.com]

When $S \subset \mathbb{R}^{N_\theta}$ is the set such that $\theta \geq \theta_{\text{crit}}$, then the projection operator $\text{Pr} : \mathbb{R}^{N_\theta} \rightarrow S^{51}$ yields the closest feasible point to $y := \theta_k^j + \nabla_\theta \log \Pi_{\text{post}}(\theta_k^j)$ by solving

$$\min_{\theta \in S} \frac{1}{2} \|\theta - y\|_2^2. \quad (18)$$

In this case, for any $y \notin S$, (18) returns $\theta = \theta_{\text{crit}}$. The results for the projected SVGD method can be seen in Figure 3.

4.2 | Space-dependent transpiration cooling

For model 2, four different sections are considered over the length of the interface, with two walls and two porous medium flows as it can be seen in Figure 5. As the uncertainty of the heat flux enters the temperature equations (2a) and (2b), the initial condition of (4a) is stochastic for the porous medium sections. We assume a uniformly distributed prior with $Re \sim \mathcal{U}(300, 1000)$. As two flows with different porosities are considered, two separate likelihood-functions are taken into account. The temperature constraint states that a temperature of 380 K should not be exceeded with a probability of 80%.

For reference, the posterior was computed for realizations of the Reynolds number and the stochastic variable q . Figure 4 shows the contour plot.

In Figure 5, the stochastic simulation is shown at the start time and $t = t_c$, on which the constraint is imposed for a Reynolds number $Re = 405$. It shows that the maximum temperature is clearly exceeded. In Figure 6, the expected value of the sampled Markov chains is used for the same simulation. Here, the temperature constraint is fulfilled. The posterior probability distributions are shown in Figure 7. For the gradient-based methods, the gradient in this case can be derived as

$$\begin{aligned} \nabla_{Re} \log \left(\Pi_{\text{prior}}(Re) \frac{1}{N} \prod_{i=0}^N \Pi_l(p_i | Re) \right) \\ = (\nabla_{Re} p(Re)) \cdot \left(\frac{1}{N \sigma_0^2} \sum_{i=0}^N (p_i^{\text{data}_0} - p(Re, \phi_0)) + \frac{1}{N \sigma_1^2} \sum_{i=0}^N (p_i^{\text{data}_1} - p(Re, \phi_1)) \right). \end{aligned} \quad (19)$$

Π_{post} with proj(SVGD) method for model 1

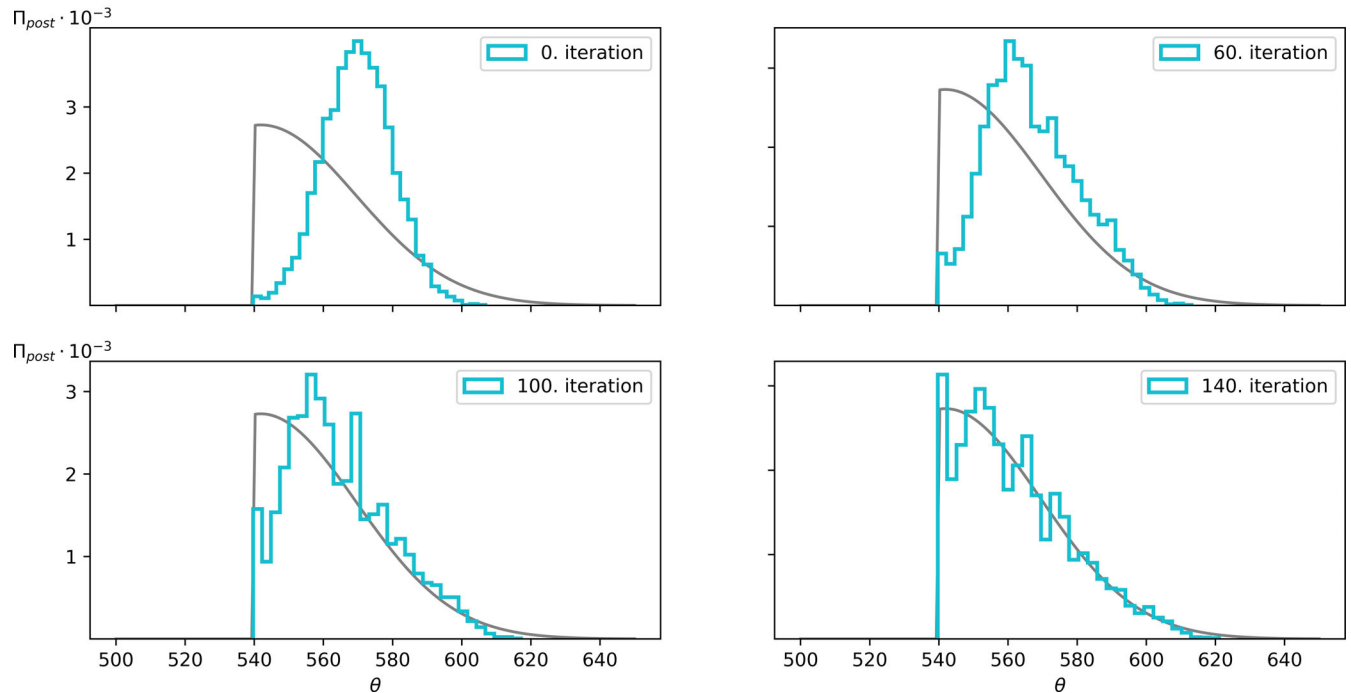


FIGURE 3 Histogram for the projected SVGD method. The evolution of the particle distribution can be seen from the initial distribution in the upper left plot over the 60th and 100th generation to the final distribution in the lower right plot. With this method, the constraint is not violated as the gradient is projected back onto the feasible region in every step. Again, the gray line shows the true posterior for comparison. [Colour figure can be viewed at wileyonlinelibrary.com]

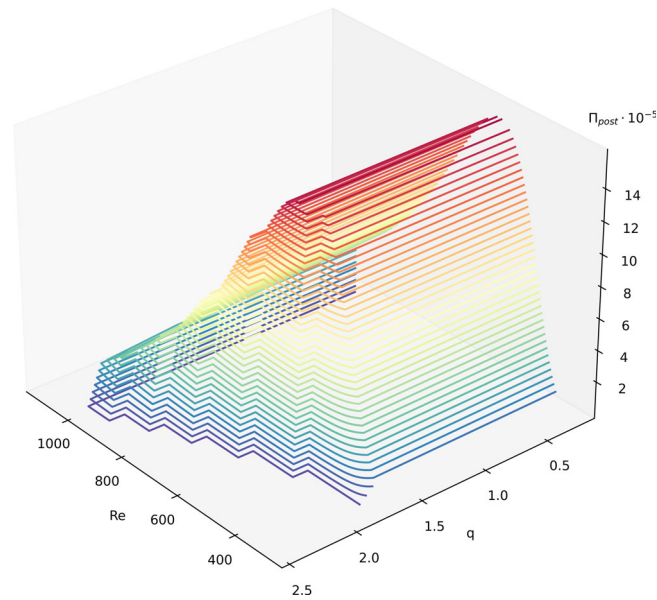


FIGURE 4 Reference posterior: Computing the constrained posterior for different realizations of the optimization parameter and the stochastic variable, it can be seen that for lower heat fluxes and higher Reynolds numbers the constraint is fulfilled, as these combinations produce lower temperatures. Here, the constraint is checked pointwise. The gPC-constraint in the sampling strategies below, however, ensures to erase any Reynolds numbers for which the probability is too high that the normally distributed heat flux results in exceeding the maximum temperature. [Colour figure can be viewed at wileyonlinelibrary.com]

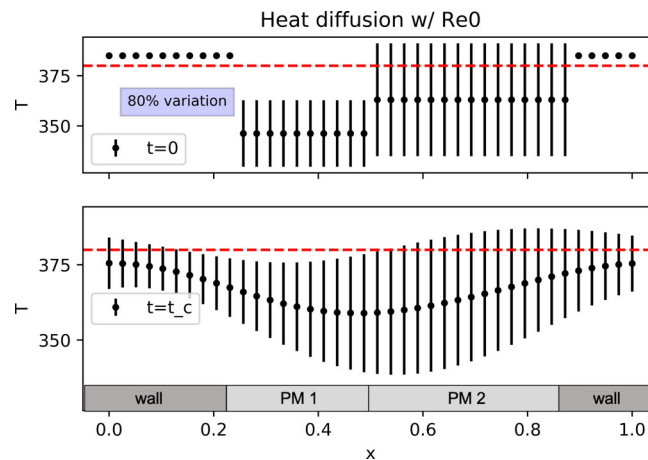


FIGURE 5 Constraint satisfaction: The temperature distribution at time $t = 0$ and $t = t_c$. The initial parameter value for the Reynolds number $Re = 405$ of the deterministic simulation (see the Appendix) was used to simulate the stochastic model. It is obvious that not only at $t = 0$ the constraint is not fulfilled, but also at $t = t_c$ the temperature still exceeds the threshold with a probability larger than 80%. [Colour figure can be viewed at wileyonlinelibrary.com]

The uniformly distributed prior with $Re \sim \mathcal{U}(300, 1000)$ is not differentiable at $Re = 400$ and $Re = 1000$. For the SVGD—that entirely relies on the gradient and the computation of the posterior probability at the particle positions itself is not part of the algorithm—an additional penalization in the same manner as for the inequality is imposed for $Re > 1000$ to avoid sampling in that region.

For the HMC, as $\log \Pi_{\text{prior}}(\theta^*) \cdot \Pi_i(\theta^*)$ at the proposal θ^* is computed for the acceptance ratio, the prior is set to be $0 < \epsilon \ll 1$ for $Re < 400$ and $Re > 1000$. In practice, this leads to a rejection of proposal candidates for $Re \notin (300, 1000)$ using the cHMC, as the probability of the posterior is nearly zero due to the extremely small ϵ .

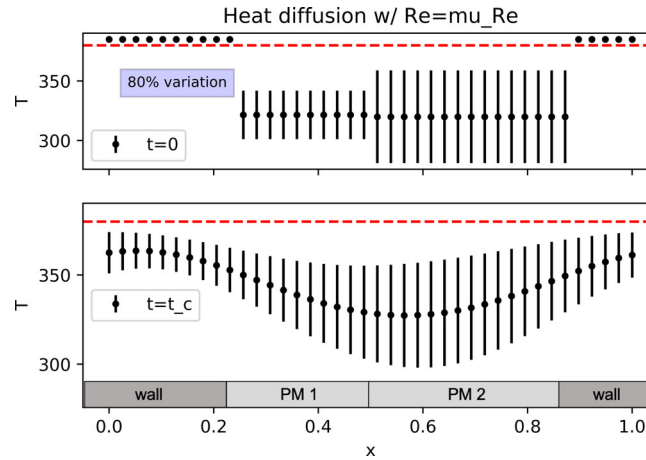


FIGURE 6 Constraint satisfaction: The same design as Figure 5 with the difference that here, the expected value of the constrained Monte Carlo methods is used to simulate the stochastic model. It can be seen that at $t = 0$ the wall temperature is above the maximum temperature while enough coolant was injected to already achieve sufficient cooling right at the outflow of the porous medium. At time $t = t_c$, the temperature is below the maximum temperature everywhere with a probability of 80%. [Colour figure can be viewed at wileyonlinelibrary.com]

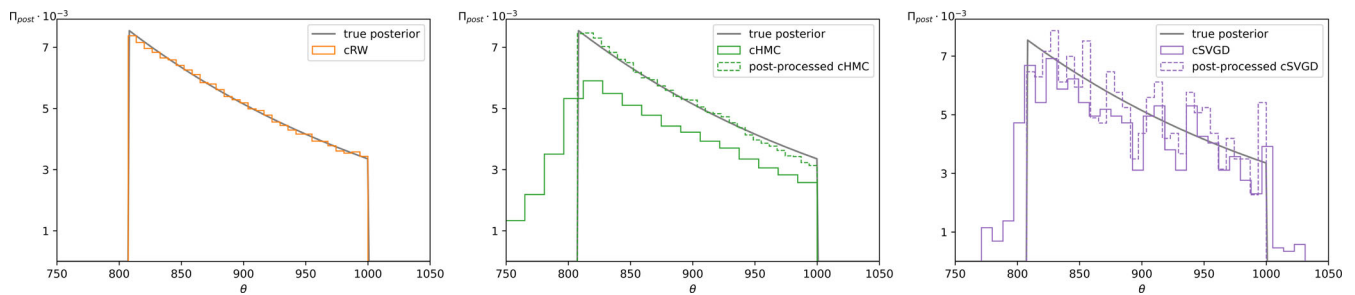


FIGURE 7 Histograms model 2: The results of the cRW, cHMC, and cSVGd, respectively. For both the cHMC and the cSVGd post-processed versions for which unfeasible samples are excluded are additionally plotted. [Colour figure can be viewed at wileyonlinelibrary.com]

4.3 | Space-dependent transpiration cooling with high-dimensional uncertain input

The space-dependent transpiration cooling model can be extended to the case with point wise uncertain heat flux over the length of the porous probe. For that, 60 independent RVs are all assumed to be normally distributed with known mean and variance according to simulation data of the heat flux from a deterministic coupled simulation setting with a hot gas flow developed in Reference 52 as it can be seen in Figure 8. The uncertainties are propagated through the pores and form the initial conditions for the heat diffusion at the interface.

The results for the cRW can be seen in Figure 9.

4.4 | Evaluation of the Monte Carlo based methods

The accuracy of the proposed methods depends on both the accuracy of the gPC expansion and the accuracy of the MCMC sampling strategies. The accuracy of the gPC expansion relate on the truncation order P which needs to be high enough so that the function f_2^P evaluated over ξ represents the true function $f_2(\xi; \theta)$.

To compare the proposed methods, however, the accuracy of the MCMC methods should be considered. Estimates of the true posterior distributions have been derived for the first and second model, where the posterior was evaluated at selected points. Therefore, a measure of accuracy is the L^2 error between the “true” posterior and the bars of the histograms. An example of the graphical evaluation can be seen in Figure 10.

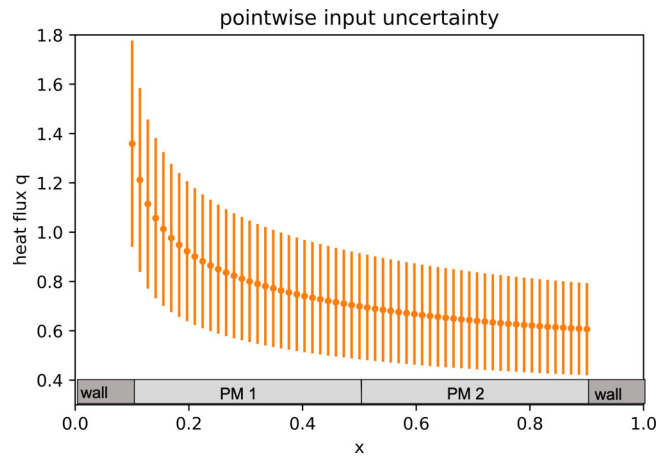


FIGURE 8 The pointwise input uncertainty of the heat flux over the interface. As the RVs are assumed to be normally distributed, mean values, and corresponding standard deviations are featured. [Colour figure can be viewed at wileyonlinelibrary.com]

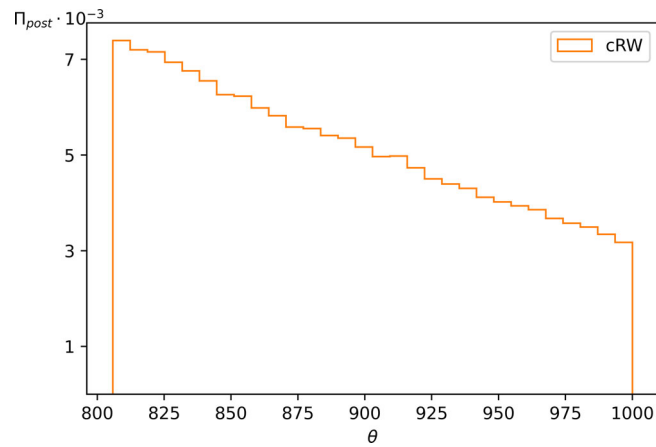


FIGURE 9 The histogram of the cRW method using 500,000 samples for model 3 is shown. Here, $S = \{806 \leq \theta \leq 1000\}$ [Colour figure can be viewed at wileyonlinelibrary.com]

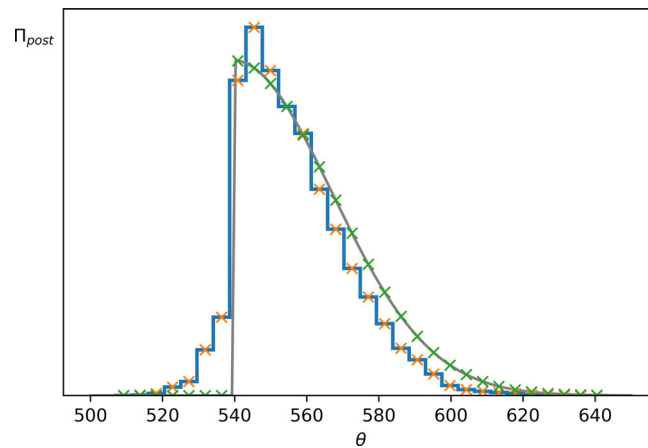


FIGURE 10 The relative L^2 error is shown. The histogram is the result of a simulation with 25,000 samples using the cHMC method for model 1. The bars of the histogram are shown with orange crosses at the middle of each bar. The corresponding point of the (estimated) true posterior is derived using interpolation (green crosses). The points are then used to compute the relative L^2 error. [Colour figure can be viewed at wileyonlinelibrary.com]

For comparability between the methods, shared measurement points are needed. Here, we choose the number of samples (N) as measurement points. This compares the end-result of the algorithms which are equally long Markov chains. For this measure, the number of samples for the particle-based SVGD are computed as the number of particles times the number of steps per particle as this the closest comparison to the overall number of samples. However, this in addition to the unused possible parallelization might unfavor the SVGD methods.

While the quality of samples might profit from the gradient-based proposal step of the cSVGd and cHMC in contrast to the random choice of the cRW, the modification still allows the cSVGd and cHMC to sample without the feasible region which is expected to negatively influence the L2 norm at the same time.

Furthermore, the evaluation of the gradient is time-consuming. It is likely that an evaluation of the gradient is dominant time-wise over the quality of the proposed sample. This is especially true in the case of cHMC, where the gradient is computed multiple times due to the number of integration steps on top of the computation of the unconstrained posterior, instead of replacing this step (as in cSVGd). Therefore, the CPU time is tracked. For the pSVGd and cSVGd the parallelization is not used such that the CPU times are comparable to the others. All instances were solved with a computer with Intel(R) Xeon 8160 CPUs with 2.10 GHz. However, we are mainly interested in the relative CPU times between the different algorithms rather than absolute CPU times.

All in all, the comparison yields in the trade-off between costly, but well-selected candidates and fast, but random suggestions in the constrained case.

The results are shown for model 1 and model 2 in Figure 11. While all methods converge for very high number of samples, the cRW shows the smallest error. For the cSVGd and cHMC the post-processed chains, where all nonfeasible samples are removed, are shown additionally. It can be seen that the performance does indeed increase when the nonfeasible samples are removed.

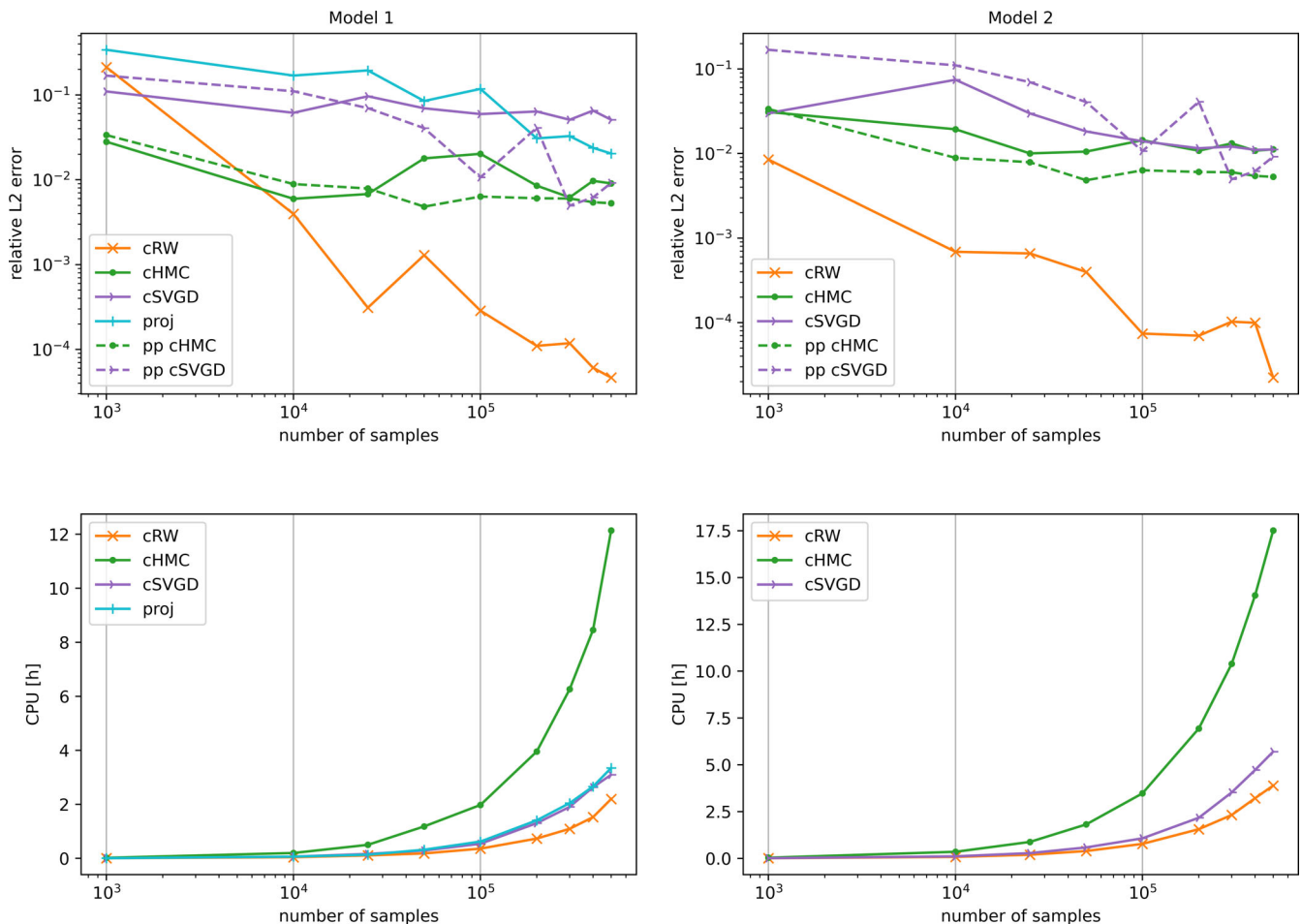


FIGURE 11 The relative error over the number of samples for model 1 on the left and model 2 on the right. The associated CPU times are shown for each method, respectively. [Colour figure can be viewed at wileyonlinelibrary.com]

The SVGD and projected SVGD require a higher number of repetitions. Their performance might be underrepresented here, as the number of particles and the number of steps need to be balanced such that they compare to the number of suggested candidates. They do perform well when using a higher number of particles, which could be iterated in parallel. However, as they do not include a rejection step, this might be the best method to compare them to the other constrained methods.

A comparison of the CPU times shows that the cHMC takes considerably longer than the other methods. Therefore, the quality gain from the gradient-information in the HMC does not automatically make it a favorable option.

The choice of hyperparameters influences the performance of the algorithms. For cRW, this is the variance of the random walk. For the cHMC, the momentum, step size, number of LeapFrog steps and the penalization parameter δ need to be tuned. The Python SVGD algorithm provided by Li already contains a step size adaption methods, such only the initial step size, and not a step size in each iteration of the particles, needs to be chosen. Furthermore, for the constrained case, the penalization parameter needs to be adapted. For the second model there are two penalizations, as the uniform prior imposes an additional constraint for $\theta > 1000$, which needs to be integrated into the SVGD framework.

It is difficult to avoid this source of bias on the performance, as the hyperparameters can only be adjusted as “optimal” as possible for each method, however their fitness is not comparable between the different algorithms. Moreover, as no specific tuning recommendations exist for constrained MCMC methods, the choice of the penalization parameter remains subjective, where the only qualitative criteria is the desired strictness of the constraint fulfillment. This might be highlighted as a key advantage of the cRW, where this is not an issue.

Furthermore, common hyperparameter adaption methods can of course be used, however their interference with the constraint are not necessarily clear. All in all, the cRW and the cSVGd with one and two hyperparameters, respectively, seem to be favorable over the cHMC with respect to the hyperparameter selection.

For this analysis, the hyperparameters were tuned for each method and model using the knowledge of the “true” posterior using brute-force optimization. The grid was refined in those regions that showed good results regarding the discussed L^2 error. For the third model, where the true posterior is not available, the analysis from Brooks and Gelman⁵³ is described below. More efficient optimization strategies might be employed in the future, however in case of the cHMC and cSVGd those need to take into account the interplay of the hyperparameters. For example, a larger step size calls for a weaker modification parameter as otherwise the edge of the feasible region is not sampled correctly. Furthermore, for the cHMC and cSVGd the distribution of the post-processed samples rather than the whole Markov chain was used to choose optimal hyperparameters. However, it should be stressed that the performances of the algorithms are highly influenced by the parameter choices, and that this puts a unresolvable bias on the direct comparison.

Overall, the cRW shows the best results taking into account the overall performance, quality stability of the proposed candidates with respect to the constrained case and CPU time. As only one hyperparameter is in need of tuning, the required model-specific adjusting of the method is small. The cSVGd, even if not proven best performance comparatively, also has strong potential when used with many particles in parallel which is especially appealing for models with high computational effort. The cHMC, even though providing good results when tuned correctly, has proven to be both very time-costly and hyperparameter sensitive. Therefore, further diagnostics for the cRW are given in the following.

For the general case, in which the true posterior is unknown, different convergence diagnostics exist to assess the convergence of the Markov chain to the stationary distribution. Often these approaches concentrate on the convergence of either the mean and variance or confidence intervals. As the shape of the posterior is non-normally in this case, sample-based confidence interval approaches can describe the overall performance better than tracking the first two statistical moments.

Brooks and Gelman⁵³ propose using diagnostics involving multiple simulations, including a sample-based confidence interval approach. Here, the confidence interval is derived using two ways: First, the mean of the within-sequence confidence intervals is computed repeatedly with an increased number of samples. Second, the mean of the total-length confidence interval using multiple chains is tracked. Convergence is suggested when the ratio of the means approaches 1 as it indicates that the confidence interval computed using the single Markov chain matches the confidence interval that is based on the full information. For further exemplifications, please see Reference 53.

The results of the method from Brooks and Gelman can be seen in Figure 12 for the cRW for model 2 and 3. It shows, that the single chain only has to contain around 1000 samples for both models for the ratio approaching 1. The results show that the cRW method still provides a converging Markov chain for a model with multiple uncertain inputs.

All three algorithms discussed here require model evaluations for the computation of the likelihood function which often comes with significant computational cost. Moreover, the SVGD and HMC rely on geometric information of the

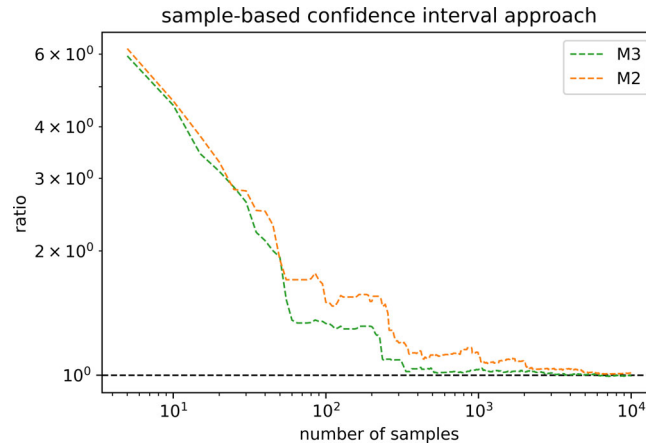


FIGURE 12 The confidence interval based approach by Brooks and Gelman for the second (orange) and third (green) model. The ratio of the 95% confidence interval of a single Markov chain to the result using two independent Markov chains of 500k samples is computed. [Colour figure can be viewed at wileyonlinelibrary.com]

posterior which might not be available for all problems. Therefore, further developments to reduce the cost of the proposed constrained algorithms could be an interesting question for future work. Starting points for this could be, for example, the work from Yan and Zhou⁵⁴ who use multi-fidelity gPC meta-models to accelerate the sampling process. Here, the gPC expansion is first based on the prior information and then adapted based on high-fidelity model evaluations. To further address the curse of dimension, they also propose to use a multi-fidelity neural-network approach, where high-fidelity simulation data and a neural network trained on prior information becomes an input to the refined neural network.⁵⁵ Lan et al.⁵⁶ propose a Gaussian Process emulator for estimation of the geometric information. Furthermore, the SVGD method can be sped up using, for example, model reduction techniques⁵⁷ and deep neural networks.⁵⁸

5 | CONCLUSION

This work is motivated by transpiration cooling for rocket thrust chambers, where the cooling technique is used to reduce thermal loads of the combustion chamber walls. While being a promising cooling technique, the multiple factors influencing transpiration cooling challenge successful simulation, which motivates the integration of parametric uncertainties into the modeling.

An approach is presented that extends Bayesian Inversion to the probabilistic constrained case using gPC and Monte Carlo based methods to solve constrained inverse problems. The fusion enables a close monitoring of the system's critical response, the temperature, by a gPC expansion of the stochastic temperature system while at the same time leveraging the access to inverse problems through the Bayesian framework.

This setting is put into use to constrain three sampling strategies, the RW, the HMC, and the SVGD. The results of the one-dimensional and two-dimensional models show that the extended strategies successfully sample the constrained target measure and the framework can be extended to different models and constraint requirements. The proposed cRW shows a strong performance compared to the other methods in terms of the overall decrease of the L^2 error over the size of the Markov chain, as well as quality stability of the proposed candidates with respect to the constrained case and CPU time.

To evaluate the chance constraint, a quantile of the temperature distribution needs to be estimated. Future work will deal with questions on how to improve the accuracy and efficiency of especially high quantile estimates. Extensions of the proposed probabilistic method to coupled simulations of the porous medium with a hot gas flow will be studied.

ACKNOWLEDGMENTS

The authors thank the Deutsche Forschungsgemeinschaft (DFG, German Research Foundation) for the financial support through 320021702/GRK2326, 333849990/IRTG-2379, CRC1481, TRR40, HE5386/18-1, 19-2, 22-1, 23-1, under Germany's

Excellence Strategy EXC-2023 Internet of Production 390621612, and under the Excellence Strategy of the Federal Government and the Länder.

This work was partially funded by the National Science Foundation awards NSF-OAC-2212442, NSF-2108320, NSF-1808576, and NSF-CAREER-1845799; by the Department of Energy award DE-SC0018147 and DE-26083989; and by 2020 ConTex award; and by 2021 UT-Portugal CoLab award. Open Access funding enabled and organized by Projekt DEAL.

DATA AVAILABILITY STATEMENT

The data that support the findings of this study are available from the corresponding author upon reasonable request.

ENDNOTE

*The Reynolds number $Re := \frac{m\dot{L}}{A\mu}$ for \dot{m} , L , A , μ corresponds to the mass flow in the dimensionless system.

ORCID

Ella Steins  <https://orcid.org/0000-0002-1615-494X>

Siegfried Müller  <https://orcid.org/0000-0001-5489-8627>

REFERENCES

1. Arai M, Suidzu T. Porous ceramic coating for transpiration cooling of gas turbine blade. *J Therm Spray Technol*. 2013;22(5):690-698.
2. Esser B, Barcena J, Kuhn M, et al. Innovative thermal management concepts and material solutions for future space vehicles. *J Spacecr Rocket*. 2016;53(6):1051-1060.
3. Langener T. *A Contribution to Transpiration Cooling for Aerospace Applications using CMC Walls*. PhD thesis. Universität Stuttgart, 2011.
4. Strauss F, Witte J, Manfletti C, Schlechtriem S. Experiments on nitrogen and hydrogen transpiration cooling in supersonic combustion ramjets (Scramjets). Space propulsion 2018; 2018. SP2018_00113.
5. Dahmen W, Gotzen T, Müller S, Rom M. Numerical simulation of transpiration cooling through porous material. *J Numer Meth Fluids*. 2014;76(6):331-365.
6. Huang G, Zhu Y, Liao Z, Ouyang X-L, Jiang P-X. Experimental investigation of transpiration cooling with phase change for sintered porous plates. *Int J Heat Mass Transf*. 2017;114:1201-1213.
7. Böhrk H. Transpiration cooling at hypersonic flight-AKTiv on SHEFEX II. Proceedings of the 11th AIAA/ASME Joint Thermophysics and Heat Transfer Conference; 2014; 2676.
8. Eckert E, Livingood N. Comparison of effectiveness of convection-, transpiration-, and film-cooling methods with air as coolant. Technical report, National advisory committee for aeronautics; 1954.
9. Selzer M, Langener T, Hald H, von Wolfersdorf J. Production and characterization of porous C/C material. Sonderforschungsbereich Transregio 40—Annual Report 2009; 2009.
10. Wang J, Messner J, Stetter H. An experimental investigation on transpiration cooling part ii: comparison of cooling methods and media. *Int J Rotat Mach*. 2004;10(5):355-363.
11. Böhrk H, Piol O, Kuhn M. Heat balance of a transpiration-cooled heat shield. *J Thermophys Heat Transf*. 2010;24(3):581-588.
12. Ding R, Wang J, He F, Dong G, Tang L. Numerical investigation on the performances of porous matrix with transpiration and film cooling. *Appl Therm Eng*. 2019;146:422-431.
13. Leontiev A, Saveliev A, Kichatov B, Kiverin A, Korshunov A, Sudakov V. Effect of gaseous coolant temperature on the transpiration cooling for porous wall in the supersonic flow. *Int J Heat Mass Transf*. 2019;142:118433.
14. Christopher N, Peter J, Kloker M, Hickey J-P. DNS of turbulent flat-plate flow with transpiration cooling. *Int J Heat Mass Transf*. 2020;157:119972.
15. Reimer T, Kuhn M, Gülhan A, Esser B, Sippel M, van Foreest A. Transpiration cooling tests of porous CMC in hypersonic flow. Proceedings of the 17th AIAA International Space Planes and Hypersonic Systems and Technologies Conference; 2011; 2251.
16. Selzer M, Schweikert S, Hald H. Throughflow characteristics of C/C. Sonderforschungsbereich Transregio 40—Annual report; 2014.
17. Wu N, Wang J, He F, Chen L, Ai B. Optimization transpiration cooling of nose cone with non-uniform permeability. *Int J Heat Mass Transf*. 2018;127:882-891.
18. Huang G, Min Z, Yang L, Jiang P-X, Chyu M. Transpiration cooling for additive manufactured porous plates with partition walls. *Int J Heat Mass Transf*. 2018;124:1076-1087.
19. Min Z, Huang G, Parbat S, Yang L, Chyu M. Experimental investigation on additively manufactured transpiration and film cooling structures. *J Turbomach*. 2019;141(3):031009.
20. Liu Y-Q, Xiong Y-B, Jiang P-X, Wang Y-P, Sun J-G. Effects of local geometry and boundary condition variations on transpiration cooling. *Int J Heat Mass Transf*. 2013;62:362-372.
21. Wilcox D. *Turbulence Modeling for CFD*. DCW Industries Inc; 2006.
22. König V, Rom M, Müller S. Ch. 2. A coupled two-domain approach for transpiration cooling. *Future Space-Transport-System Components Under High Thermal and Mechanical Loads: Results from the DFG Collaborative Research Center TRR40*. Springer; 2021:33-49.

23. Cerminara A, Deiterding R, Sandham N. Direct numerical simulation of hypersonic flow through regular and irregular porous surfaces. *Proceedings of the 7th European Conference on Computational Fluid Dynamics*; 2019.
24. Sudret B. Global sensitivity analysis using polynomial chaos expansions. *Reliab Eng Syst Saf*. 2008;93(7):964-979.
25. Wiener N. The homogeneous chaos. *Am J Math*. 1938;60(4):897-936.
26. Cameron R, Martin W. The orthogonal development of non-linear functionals in series of Fourier-Hermite functionals. *Ann Math*. 1947;48(2):385-392.
27. Ghanem R, Spanos P. Stochastic finite element method: response statistics. *Stochastic Finite Elements: A Spectral Approach*. Springer; 1991:101-119.
28. Ghanem R. Probabilistic characterization of transport in heterogeneous media. *Comput Methods Appl Mech Eng*. 1998;158(3-4):199-220.
29. Xiu D, Karniadakis G. The Wiener-Askey polynomial chaos for stochastic differential equations. *SIAM J Sci Comput*. 2002;24(2):619-644.
30. Sullivan T. *Introduction to Uncertainty Quantification*. Springer; 2015.
31. Gerster S, Herty M, Sikstel A. Hyperbolic stochastic Galerkin formulation for the P-system. *J Comput Phys*. 2019;395:186-204.
32. Mackay D. Introduction to Monte Carlo methods. *Learning in Graphical Models*. Springer; 1998:175-204.
33. Xiu D, Hesthaven J. High-order collocation methods for differential equations with random inputs. *SIAM J Sci Comput*. 2005;27(3):1118-1139.
34. Berveiller M, Sudret B, Lemaire M. Stochastic finite element: a non intrusive approach by regression. *Eur J Comput Mech/Revue Européenne de Mécanique Numérique*. 2006;15(1-3):81-92.
35. Blatman G, Sudret B. An adaptive algorithm to build up sparse polynomial chaos expansions for stochastic finite element analysis. *Probab Eng Mech*. 2010;25(2):183-197.
36. Calvetti D, Somersalo E. Inverse problems: from regularization to Bayesian inference. *Wiley Interdiscipl Rev Comput Stat*. 2018;10(3):e1427.
37. Brooks S, Gelman A, Jones G, Meng X. *Handbook of Markov Chain Monte Carlo*. CRC Press; 2011.
38. Cappé O, Godsill S, Moulines E. An overview of existing methods and recent advances in sequential Monte Carlo. *Proc IEEE*. 2007;95(5):899-924.
39. Kaipio J, Somersalo E. *Statistical and Computational Inverse Problems*. Springer-Verlag; 2005:0066-5452.
40. Wang Z, Mohamed S, Freitas N. Adaptive Hamiltonian and Riemann manifold Monte Carlo. *Proceedings of the International Conference on Machine Learning*; 2013:1462-1470; PMLR.
41. Liu Q, Wang D. Stein variational gradient descent: a general purpose Bayesian inference algorithm. arXiv preprint arXiv:1608.04471, 2016.
42. Wu J, Wang J, Shadden S. Adding constraints to Bayesian inverse problems. *Proceedings of the 33rd AAAI Conference on Artificial Intelligence (AAAI-19)*; 2019.
43. Frazier P. A tutorial on Bayesian optimization. arXiv:1807.02811, 2018.
44. Gardner J, Kusner M, Xu Z, Weinberger K, Cunningham J. Bayesian optimization with inequality constraints. *Proceedings of the 31st International Conference on Machine Learning, Beijing, China, 2014*.
45. Gelbart M. *Constrained Bayesian Optimization and Applications*. PhD thesis, Harvard University, 2015.
46. Müller S, Rom M. Analytical investigations of 1D Darcy-Forchheimer flow under local thermal non-equilibrium. IGPM preprint 521, RWTH Aachen; 2022.
47. Rom M, Müller S. Derivation and analysis of a 1D porous medium flow solver embedded in a two-domain model for 2D and 3D transpiration cooling. *Int J Heat Mass Transf*. 2022;195:123127.
48. Peichl J, Schwab A, Selzer M, Böhrk H, von Wolfersdorf J. *Innovative Cooling for Rocket Combustion Chambers*. Springer; 2021:51-64.
49. Lu F, Morzfeld M, Tu X, Chorin A. Limitations of polynomial chaos expansions in the Bayesian solution of inverse problems. *J Comput Phys*. 2015;282:138-147.
50. Calvetti D, Somersalo E. *Introduction to Bayesian Scientific Computing*. Springer; 2007.
51. Burke J. The gradient projection algorithm. *Lecture notes at the University of Washington*; 2014.
52. Dahmen W, Müller S, Rom M, Schweikert S, Selzer M, von Wolfersdorf J. Numerical boundary layer investigations of transpiration-cooled turbulent channel flow. *Int J Heat Mass Transf*. 2015;86:90-100.
53. Brooks S, Gelman A. General methods for monitoring convergence of iterative simulations. *J Comput Graph Stat*. 1998;7(4):434-455.
54. Yan L, Zhou T. Adaptive multi-fidelity polynomial chaos approach to Bayesian inference in inverse problems. *J Comput Phys*. 2019;381:110-128.
55. Liang Y, Zhou T. An adaptive surrogate modeling based on deep neural networks for large-scale Bayesian inverse problems. arXiv preprint arXiv:1911.08926, 2019.
56. Lan S, Tan B-T, Christie M, Girolami M. Emulation of higher-order tensors in manifold Monte Carlo methods for Bayesian inverse problems. *J Comput Phys*. 2016;308:81-101.
57. Chen P, Ghattas O. Stein variational reduced basis Bayesian inversion. *SIAM J Sci Comput*. 2021;43(2):A1163-A1193.
58. Yan L, Zhou T. Stein variational gradient descent with local approximations. *Comput Methods Appl Mech Eng*. 2021;386:114087.

How to cite this article: Steins E, Bui-Thanh T, Herty M, Müller S. Probabilistic constrained Bayesian inversion for transpiration cooling. *Int J Numer Meth Fluids*. 2022;1-20. doi: 10.1002/flid.5135

APPENDIX

TABLE A1 Deterministic parameter set (with dimensions)

Parameter	Symbol	Value
Reynolds number	Re	$Re_0 = 405$
Prandtl number	Pr_f	0.64
Nusselt number	$Nu_{v,f}$	7500
Heat flux	q	$q_0 = 30,845 \text{ W/m}^2$
Hot gas temperature	T_{HG}	347 K
Porosity	ϕ	$\phi_0 = 0.111, \phi_1 = 0.4$
Thermal conductivity of fluid	κ_f	0.03 W/(m K)
Thermal conductivity of solid	κ_s	15.2 W/(m K)
Permeability	K_D	$3.57\text{e}-13 \text{ m}^2$
Forchheimer coefficient	K_F	$5.17\text{e}-08 \text{ m}$
Coolant reservoir temperature	T_c	304.2 K
Solid reservoir temperature	T_b	321.9 K
Reservoir pressure	p_R	600,000 Pa
Length of the porous medium	L	0.015 m